THE JOURNAL OF BIOLOGICAL CHEMISTRY VOL. 283, NO. 16, pp. 11024–11037, April 18, 2008
Printed in the U.S.A.

Solution NMR Structures of Productive and Non-productive Complexes between the A and B Domains of the Cytoplasmic Subunit of the Mannose Transporter of the *Escherichia coli* Phosphotransferase System*

Received for publication, January 11, 2008 Published, JBC Papers in Press, February 11, 2008, DOI 10.1074/jbc.M800312200

Jun Hu[1], **Kaifeng Hu**[1], **David C. Williams, Jr.**[2], **Michal E. Komlosh**[3], **Mengli Cai, and G. Marius Clore**[4]
From the Laboratory of Chemical Physics, NIDDK, National Institutes of Health, Bethesda, Maryland 20892

Solution structures of complexes between the isolated A (IIA^{Man}) and B (IIB^{Man}) domains of the cytoplasmic component of the mannose transporter of *Escherichia coli* have been solved by NMR. The complex of wild-type IIA^{Man} and IIB^{Man} is a mixture of two species comprising a productive, phosphoryl transfer competent complex and a non-productive complex with the two active site histidines, His-10 of IIA^{Man} and His-175 of IIB^{Man}, separated by ~25 Å. Mutation of the active site histidine, His-10, of IIA^{Man} to a glutamate, to mimic phosphorylation, results in the formation of a single productive complex. The apparent equilibrium dissociation constants for the binding of both wild-type and H10E IIA^{Man} to IIB^{Man} are approximately the same (K_D ~ 0.5 mM). The productive complex can readily accommodate a transition state involving a pentacoordinate phosphoryl group with trigonal bipyramidal geometry bonded to the Nε2 atom of His-10 of IIA^{Man} and the Nδ1 atom of His-175 of IIB^{Man} with negligible (<0.2 Å) local backbone conformational changes in the immediate vicinity of the active site. The non-productive complex is related to the productive one by a ~90° rotation and ~37 Å translation of IIB^{Man} relative to IIA^{Man}, leaving the active site His-175 of IIB^{Man} fully exposed to solvent in the non-productive complex. The interaction surface on IIA^{Man} for the non-productive complex comprises a subset of residues used in the productive complex and in both cases involves both subunits of IIA^{Man}. The selection of the productive complex by IIA^{Man}(H10E) can be attributed to neutralization of the positively charged Arg-172 of IIB^{Man} at the center of the interface. The non-productive IIA^{Man}-IIB^{Man} complex may possibly be relevant to subsequent phosphoryl transfer from His-175 of IIB^{Man} to the incoming sugar located on the transmembrane IIC^{Man}-IID^{Man} complex.

The bacterial phosphoenolpyruvate:sugar phosphotransferase system (PTS)[5] is a phosphorylation cascade involved in active sugar transport, signaling, and the regulation of carbon catabolite repression as well as an array of other cellular processes (1–3). The initial phosphorylation steps from phosphoenolpyruvate to His-189 (Nε2) of enzyme I and subsequently to His-15 (Nδ1) of HPr are common to all branches of the PTS. Thereafter, the phosphoryl group is transferred to sugar-specific enzymes II, which fall into four major families, glucose (Glc), mannitol (Mtl), mannose (Man), and chitobiose (Chb). The enzymes II are organized into two cytoplasmic domains A and B, and one or two membrane-bound domains, C and D, which may or may not be covalently linked to one another. The A domains from the four major families bear no sequence or structural similarity to one another, but in all cases the active site residue is a histidine (Nε2) that accepts a phosphoryl group from His-15 (Nδ1) of HPr and donates a phosphoryl group to either a cysteine residue in the case of IIB^{Glc}, IIB^{Mtl}, and IIB^{Chb} or a histidine residue (Nδ2) for IIB^{Man}. As in the case of the A domains, the B domains from the four major families bear no sequence similarity to one another, and with the exception of IIB^{Mtl} (4) and IIB^{Chb} (5), which have similar topologies, bear no structural similarity either (2, 3).

The various protein-protein complexes of the PTS provide a paradigm to explore the structural basis of protein-protein interactions and the factors that permit the recognition of diverse partners using structurally similar interfaces. Moreover, the complexes of the PTS are generally weak (K_D ranging from the micromolar to millimolar range) and to date have proved refractory to crystallization. In a series of reports we have used NMR spectroscopy to solve the structures of complexes of HPr with the N-terminal domain of enzyme I (6), IIA^{Glc} (7), IIA^{Mtl} (8), and IIA^{Man} (9), and complexes of IIA^{Glc} and IIA^{Mtl} with IIB^{Glc} (10) and IIB^{Mtl} (11), respectively. In this report we explore the interaction of the IIA^{Man} dimer (35 kDa) with IIB^{Man} (19 kDa), thereby completing the structure determination of the cytoplasmic complexes of the mannose branch of the *E. coli* PTS.

The mannose transporter of *E. coli* comprises four domains, expressed as three proteins: $IIAB^{Man}$, IIC^{Man}, and IID^{Man} (12, 13).

* This work was supported by the intramural program of NIDDK, National Institutes of Health (NIH), and the Intramural AIDS Targeted Antiviral Program of the Office of the Director of the NIH (to G. M. C.). The costs of publication of this article were defrayed in part by the payment of page charges. This article must therefore be hereby marked "*advertisement*" in accordance with 18 U.S.C. Section 1734 solely to indicate this fact.

The atomic coordinates and experimental NMR restraints (codes 2JZH, 2JZN, 2JZO, and 1VSQ) have been deposited in the Protein Data Bank, Research Collaboratory for Structural Bioinformatics, Rutgers University, New Brunswick, NJ (http://www.rcsb.org/).

[1] Both authors contributed equally to this work.

[2] Present address: Dept. of Pathology, Virginia Commonwealth University, Richmond, VA 23298-0662.

[3] Present address: NICHD, NIH, Bethesda, MD 20892.

[4] To whom correspondence should be addressed: Laboratory of Chemical Physics, Bldg. 5, Rm. B1-30I, NIDDK, NIH, Bethesda, MD 20892-0520. Tel.: 301-496-0782; Fax: 301-496-0825; E-mail: mariusc@intra.niddk.nih.gov.

[5] The abbreviations used are: PTS, phosphoenolpyruvate:sugar phosphotransferase system; HPr, histidine-containing phosphocarrier protein; $IIAB^{Man}$, the cytoplasmic subunit of the mannose transporter; IIC^{Man}-IID^{Man} complex, transmembrane component of the mannose transporter; Man, mannose; Glc, glucose; Mtl, mannitol; Chb, chitobiose; NOE, nuclear Overhauser effect; HMQC, heteronuclear multiple quantum coherence; HSQC, heteronuclear single quantum coherence; RDC, residual dipolar coupling; r.m.s., root mean square.

The two transmembrane components, IIC^{Man} and IIB^{Man}, form a tight complex (13). The cytoplasmic component, IIAB^{Man}, is an obligate dimer with all dimerization contacts mediated by the A domain (14–16). The A (residues 1–134) and B (residues 160–323) domains of IIAB^{Man} are covalently attached by a flexible 25-residue alanine/proline-rich linker (residues 135–159) and fold independently of one another (15). Phosphoryl transfer occurs between His-10 of IIA^{Man} and His-175 of IIB^{Man} (14, 17). In the homologous sorbose (II^{Sor}) permease of *Klebsiella pneumoniae* (18) and fructose (II^{Lev}) permease of *Bacillus subtilis* (19), the A and B domains are expressed as separate polypeptide chains. To simplify the NMR spectroscopy and facilitate the identification of intermolecular contacts through isotope-filtered/separated nuclear Overhauser enhancement (NOE) experiments we therefore chose to carry out structural work on complexes of isolated IIA^{Man} and IIB^{Man}.

A high (1.7 Å) resolution crystal structure of *E. coli* IIA^{Man} had previously been solved, but no structure was available for IIB^{Man}. We therefore first solved the solution structure of *E. coli* IIB^{Man} on the basis of NOE and dipolar coupling data in two alignment media, and then used this structure together with the x-ray structure of IIA^{Man} to solve the structure of the IIA^{Man}-IIB^{Man} complex by conjoined rigid body/torsion angle dynamics on the basis of intermolecular NOE data. The intermolecular data recorded on the wild-type IIA^{Man}-IIB^{Man} complex were not compatible with the existence of a single species. Subsequent mutation of the active site His-10 of IIA^{Man} to Glu to mimic phosphorylation of His-10 resulted in the formation of a single complex that was fully consistent with the stereochemical and geometric requirements for phosphoryl transfer between His-10 of IIA^{Man} and His-175 of IIB^{Man}. Selection of a single complex by the H10E mutation is due to neutralization of the positively charged Arg-172 of IIB^{Man} at the center of the protein-protein interface of the productive complex. With the structure of the productive complex in hand, we were then able to determine the structure of the non-productive complex by accounting for the intermolecular NOE data on the basis of a mixture of productive and non-productive complexes. In the non-productive complex the active site histidines of IIA^{Man} and IIB^{Man} are ~25 Å apart, and the active site His-175 and associated active site loop of IIB^{Man} are exposed to solvent. We suggest that the non-productive complex may therefore be relevant to subsequent phosphoryl transfer to the incoming sugar located on the cytoplasmic side of the transmembrane IIC^{Man}-IID^{Man} complex. This study illustrates how, for weak protein-protein complexes, a relatively subtle change in a single interfacial residue can have a dramatic impact on the configuration of the resulting complex that, in this instance, may play an important role in both modulating and directing the phosphorylation cascade within the mannose transporter.

EXPERIMENTAL PROCEDURES

Cloning, Expression, and Purification of IIA^{Man} and IIB^{Man}—The A domain of wild-type IIAB^{Man} (residues 1–136, IIA^{Man}) of *E. coli* was expressed and purified as described previously (9).

The DNA corresponding to the B domain of IIAB^{Man} (residues 157–323, IIB^{Man}) was amplified by PCR using a DNA template derived from *E. coli* chromosomal DNA provided by A. Peterkofsky. The PCR product contains an NcoI restriction site at the 5′ site and a tandem pair of in-frame termination codons and a BamHI site at the 3′ site introduced during the PCR reaction. The NcoI- and BamHI-cut PCR product was purified and subcloned into the corresponding expression sites of the modified pET32a vector (4) to form a thioredoxin fusion protein with a His_6 tag. The selected clone was verified by DNA sequencing.

The following mutations, H10E in IIA^{Man}, and R172Q and H175E in IIB^{Man} were introduced using the QuikChange mutagenesis kit (Stratagene), and the sequences confirmed by DNA sequencing. Expression and purification was carried out using the same protocols as that for the corresponding wild-type proteins.

The plasmids for IIA^{Man} and IIB^{Man} were introduced into *E. coli* BL21(DE3) (Novagen) cells for protein expression and induced at an A_{600} ~ 0.8 with 1 mM isopropyl-β-D-thiogalactopyranoside at 37 °C and 30 °C, respectively. Cells were grown in either Luria-Bertani medium or minimal media (in either H_2O or D_2O, with $^{15}NH_4Cl$ or $^{14}NH_4Cl$, and [U-^{13}C/^{1}H]-, [U-^{12}C/^{1}H]-, [U-^{13}C/^{2}H]-, or [U-^{12}C/^{2}H]glucose as the main nitrogen and carbon sources, respectively). Because Leu, Val, Met, and Trp residues are involved in the IIA^{Man}/IIB^{Man} interface, selective labeling was also employed in the preparation of NMR samples. For $^{15}N/^{13}C/^{2}H$-(Leu/Val)-methyl-protonated (but otherwise fully deuterated) protein samples, 100 mg of [$^{13}C_5$,3-$^{2}H_1$]α-ketoisovalerate (Cambridge Isotopes) was added to 1 liter of D_2O medium 1 h prior to induction (22). The $^{14}N/^{12}C/^{2}H$-(Leu/Val)-methyl-protonated (Trp/Met)-protonated (but otherwise fully deuterated) IIA^{Man} samples ([$^{12}CH_3$-LV]/[^{1}H-MW]/[$^{12}C/^{14}N/^{2}H$]-IIA^{Man}) were prepared by supplementing 1 liter of D_2O medium with 100 mg of [$^{12}C_5$,3-$^{2}H_1$]α-ketoisovalerate (Sigma-Aldrich), 150 mg of methionine, and 200 mg of tryptophan 1 h prior to induction.

After induction (3 and 10 h for growths in H_2O and D_2O, respectively), cells expressing IIB^{Man} protein were harvested, pelleted by centrifugation and resuspended in 50 ml (per liter of culture) of 30 mM Tris, pH 8.0, 10 mM imidazole and 200 mM NaCl. The cell suspension was lysed by three passages through a microfluidizer and centrifuged at 10,000 × *g* for 20 min. The supernatant was loaded onto a 5-ml nickel-Sepharose column (HisTrap HP, Amersham Biosciences), and the fusion protein was eluted with a 50-ml gradient of imidazole (10–500 mM). The eluted protein was collected and digested with 200 NIH units of thrombin after overnight dialysis against a 4-liter buffer of 25 mM Tris, pH 8.0, and 200 mM NaCl. Thrombin was removed by passage over a benzamidine-Sepharose column (1 ml, Amersham Biosciences), followed by the addition of 1 mM phenylmethylsulfonyl fluoride. The IIB^{Man} protein after cleavage was collected after loading the digested mixture onto a 5-ml nickel-Sepharose column and further purified by gel filtration.

All NMR samples were prepared in a buffer of 20 mM sodium phosphate, pH 6.5, 0.01% sodium azide, and either 90% H_2O/10% D_2O or 99.996% D_2O. IIA^{Man} is a symmetric dimer with two non-overlapping but equivalent binding sites for IIB^{Man}. To achieve optimal line widths we chose to record the majority of spectra on samples comprising a 1:1 mixture of IIA^{Man} dimer to IIB^{Man} monomer (see "Results" and "Discussion").

NMR Spectroscopy—NMR spectra were recorded at 30 °C on Bruker DMX500, DMX600, DRX600, and DRX800 spectrometers equipped with either *x*-, *y*-, and *z*-shielded gradient triple resonance probes or *z*-shielded gradient triple resonance cryoprobes. Spectra were processed with the NMRPipe package (23) and analyzed using the programs PIPP, CAPP, and STAPP (24).

Sequential and side-chain assignments of free IIB^{Man} were derived from three-dimensional double and triple resonance through-bond correlation experiments (25, 26): HNCACB, CBCA(CO)NH, HBHA-(CBCACO)NH, C(CCO)NH, H(CCO)NH), HCCH-COSY, and HCCH-TOCSY. Interproton distance restraints were derived from three-dimensional ^{15}N-, ^{13}C-, ^{13}C/^{15}N-, ^{13}C/^{13}C-, and ^{15}N/^{15}N-separated NOE spectra (25, 26). Side-chain rotamers were derived from $^{3}J_{NC\gamma}$ (aromatic, methyl, and methylene), $^{3}J_{C'C\gamma}$ (aromatic, methyl, and methylene) and $^{3}J_{CC}$ scalar couplings measured by quantitative J correlation spectroscopy (27), in combination with data from a short mixing time three-dimensional ^{13}C-separated NOE spectrum recorded in H_2O and a three-dimensional ^{15}N-separated ROE spectrum (26). Residual dipolar couplings (RDCs) were measured by taking the difference in J couplings between aligned and isotropic media using well established procedures (28). $^{1}D_{NH}$, $^{1}D_{NC'}$, and $^{2}D_{NC'}$ RDCs were obtained in two alignment media: 10 mg/ml phage pf1 (29) and 5% $C_{12}E_5$ polyethylene glycol/hexanol (30).

Assignments of free wild-type IIA^{Man} were taken from previously published work by Williams *et al.* (9). Assignments for the H10E mutant of IIA^{Man} were derived from three-dimensional double and triple resonance experiments with reference to the free wild-type IIA^{Man} assignments.

Assignments of ^{13}C, ^{15}N, and ^{1}H chemical shifts in the IIA^{Man}-IIB^{Man} complex were based on the assignments of the free proteins in conjunction with data from titration experiments using constant time ^{1}H-^{13}C HMQC and TROSY ^{1}H-^{15}N spectra, as well as TROSY-based triple resonance through-bond correlation experiments (31).

Intermolecular NOEs were observed on the IIA^{Man}-IIB^{Man} complex in D_2O buffer using three-dimensional ^{12}C-filtered(F_1)/^{13}C-separated(F_2) or ^{13}C-separated(F_2)/^{12}C-filtered(F_3) NOE experiments and in H_2O buffer using two-dimensional ^{15}N separated/^{13}C-edited and two-dimensional ^{13}C-separated/^{15}N-edited NOE experiments (32). The following combinations of isotope-labeled complexes were primarily used for analysis of intermolecular NOEs: [U-^{1}H/^{13}C/^{15}N]-IIB^{Man} with unlabeled IIA^{Man} (wild-type and H10E), [$^{12}CH_3$-LV]/[^{12}C/^{14}N/^{2}H]-IIA^{Man}, [$^{12}CH_3$-LV]/[^{1}H-MW]/[^{12}C/^{14}N/^{2}H]-IIA^{Man} (wild-type and H10E), and [^{1}H-M]/[^{12}C/^{14}N/^{2}H]-IIA^{Man}; unlabeled IIB^{Man} with [U-^{1}H/^{13}C/^{15}N]-IIA^{Man} (wild-type and H10E); [$^{13}CH_3$-LV]/[^{2}H/^{12}C/^{14}N]-IIB^{Man} with [$^{12}CH_3$-LV]/[^{12}C/^{14}N/^{2}H]-IIA^{Man} and [$^{12}CH_3$-LV]/[^{1}H-MW]/[^{12}C/^{14}N/^{2}H]-IIA^{Man} (wild-type and H10E); [$^{12}CH_3$-LV]/[^{2}H/^{12}C/^{14}N]-IIB^{Man} and [$^{13}CH_3$-LV]/[^{1}H/^{13}C-M]/[^{2}H/^{13}C/^{15}N]-IIA^{Man}; [U-^{1}H/^{13}C/^{15}N]-IIB^{Man}(R172Q) with ($^{12}CH_3$-LV]/[^{1}H-MW]/[^{12}C/^{14}N/^{2}H]-IIA^{Man}(H10E); [U-^{1}H/^{13}C/^{15}N]-IIB^{Man}(H175E) and [U-^{1}H/^{13}C/^{15}N]-IIB^{Man}(R172Q) with [U-^{12}C/^{14}N/^{1}H]-IIA^{Man}; and [$^{1}H_N$-^{15}N/^{12}C/^{2}H]-IIB^{Man} with [$^{13}CH_3$-LV]/[^{1}H/^{13}C-M]/[^{2}H/^{13}C/^{15}N]-IIA^{Man}(H10E).

Structure Calculations—Interproton distance restraints were derived from the NOE spectra and classified into generous approximate distance ranges, 1.8–2.7, 1.8–3.5, 1.8–5.0, and 1.8–6.0 Å (with an additional 0.5 Å added to the upper limits for NOEs involving methyl groups), corresponding to strong, medium, weak, and very weak NOE cross-peak intensities, respectively (25, 33). Non-stereospecifically assigned methyl, methylene, and aromatic protons and ambiguous intermolecular NOEs were represented by a $(\Sigma r^{-6})^{-1/6}$ sum (26, 34). ϕ/ψ torsion angle restraints for free IIB^{Man} were derived from backbone (N, C′, Cα, Cβ, and Hα) chemical shifts using the program TALOS (35). Side-chain χ torsion angle restraints were derived from ^{3}J heteronuclear couplings and short mixing time NOE and ROE experiments using standard procedures (26). The minimum range for the torsion angle restraints was ±20°.

All structure calculations were carried out using Xplor-NIH (36) and the IVM (21) module for torsion angle and rigid body dynamics. The structure of the free IIB^{Man} was calculated by simulated annealing in torsion angle space (21). The structure deter-

TABLE 1

Structural statistics for free IIB^{Man}

⟨SA⟩ are the final 130 simulated annealing structures. $(SA)_r$ is the restrained regularized mean structure derived from the mean coordinates obtained by averaging the coordinates of the 130 simulated annealing structures best-fitted to each other. The number of terms for the various experimental restraints is given in parentheses. None of the structures exhibit interproton distance violations >0.3 Å or torsion angle violations >5°.

	⟨SA⟩	$(SA)_r$
r.m.s. deviation from experimental restraints		
Distances (Å) (1577)[a]	0.006 ± 0.001	0.008
Torsion angles (°) (478)[b]	0.33 ± 0.03	0.26
$^{13}C\alpha$ shifts (ppm) (161)	1.26 ± 0.01	1.25
$^{13}C\beta$ shifts (ppm) (158)	1.24 ± 0.01	1.23
RDC *R*-factors (%)[c]		
Phage $^{1}D_{NH}$ (151)	4.3 ± 0.1	4.2
Phage $^{1}D_{NC'}$ (113)	18.7 ± 0.5	18.2
Phage $^{2}D_{HNC'}$ (113)	16.9 ± 0.2	16.5
PEG/hexanol $^{1}D_{NH}$ (141)	5.9 ± 0.1	6.0
PEG/hexanol $^{1}D_{NC'}$ (96)	26.5 ± 0.3	25.8
PEG/hexanol $^{2}D_{HNC'}$ (103)	24.3 ± 0.3	23.5
r.m.s. deviations from idealized covalent geometry		
Bonds (Å)	0.002 ± 0.0001	0.004
Angles (°)	0.36 ± 0.02	0.54
Impropers (°)	0.53 ± 0.04	0.65
Measures of structure quality[d]		
% residues in most favored region of Ramachandran plot	93.1 ± 0.7	92.6
Bad contacts per 100 residues	3.4 ± 1.0	1.8
Precision of atomic coordinates (Å)[e]		
Backbone (N, Cα, C′, and O)	0.26 ± 0.04	
All heavy atoms	0.74 ± 0.05	

[a] There are 1467 interproton distance restraints comprising 451 intra-residue restraints, and 407 $|i-j|=1$ sequential, 270 $1<|i-j|\leq 5$ medium range and 339 $|i-j|>5$ long range inter-residue restraints. In addition there are 110 distance restraints for 55 backbone hydrogen bonds that were added during the final stages of refinement.

[b] The torsion angle restraints comprise 160 ϕ, 157 ψ, 108 χ_1, 44 χ_2, and 9 χ_3 angles.

[c] The RDC *R*-factor, which scales between 0 and 100%, is defined as the ratio of the r.m.s. deviation between observed and calculated values to the expected r.m.s. deviation if the vectors were randomly distributed, given by $[2D_a^2(4+3\eta^2)/5]^{1/2}$, where D_a is the magnitude of the principal component of the alignment tensor, and η is the rhombicity (61). The values of D_a^{NH} and η, derived from the distribution of normalized RDCs, are −11.7 Hz and 0.30, respectively, for the data recorded in pf1 phage, and −10.0 Hz and 0.28, respectively, for the data in PEG/hexanol (62).

[d] Calculated with the program PROCHECK (48). The dihedral angle PROCHECK G factors for ϕ/ψ, χ_1/χ_2, χ_1, and χ_3/χ_4 are 0.06 ± 0.02, 0.57 ± 0.06, 0.14 ± 0.08, and 0.22 ± 0.13, respectively. The WHATIF first generation packing score is 0.13; a value greater than −0.5 is considered to represent a high quality structure (63).

[e] The precision of the coordinates is defined as the average atomic r.m.s. difference between the individual 130 simulated annealing structures and the corresponding mean coordinates best-fitted to the backbone atoms of residues 160–321. (Residues 156–159 and 322–323 at the N and C termini, respectively, are disordered.)

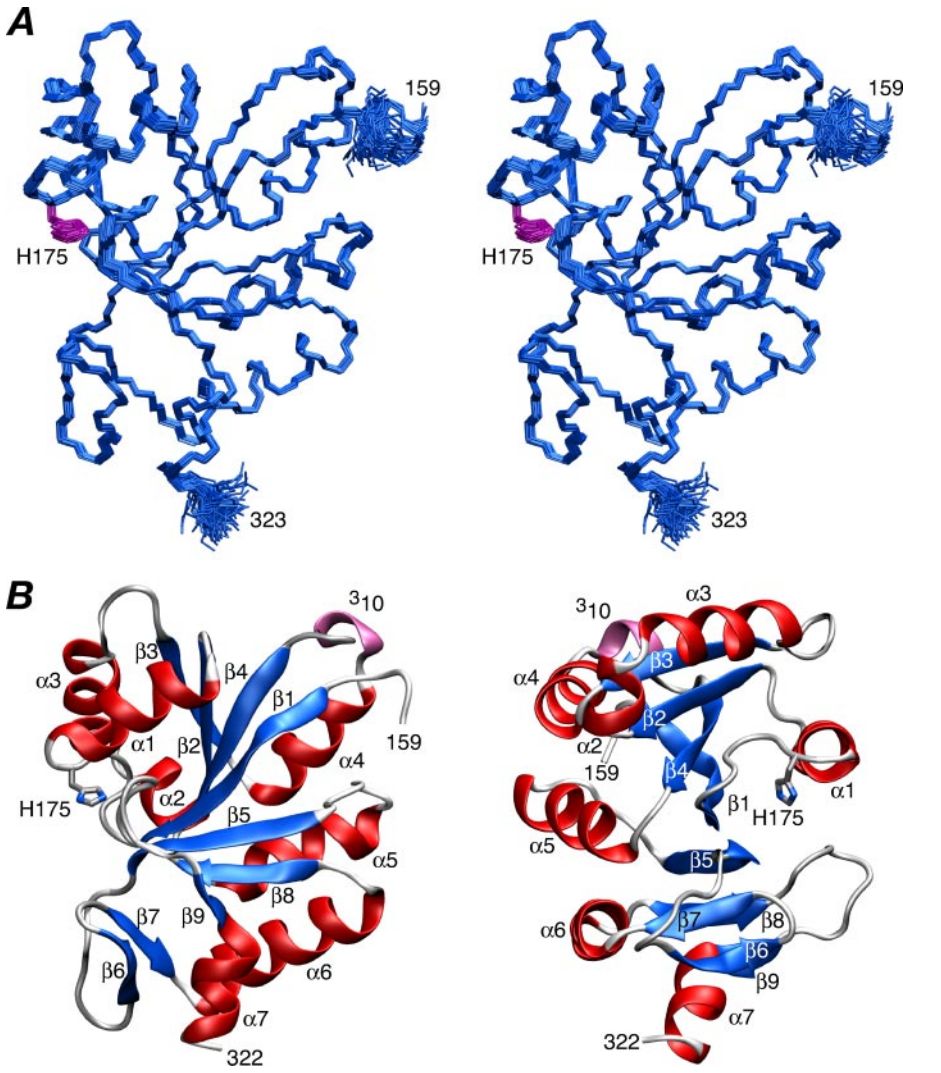

FIGURE 1. **Solution structure of IIB^{Man}.** *A*, stereoview of a best-fit superposition of 130 simulated annealing structures with the backbone (N, Cα, and C) atoms in *blue* and the side chain of the active site His-175 in *purple*. *B*, two approximately orthogonal views of a ribbon diagram of IIB^{Man} with α-helices in *red*, sheets in *blue*, and the single 3–10 helix in *lilac*.

including 1467 NOE-derived interproton distance restraints and 717 backbone RDCs ($^1D_{NH}$, $^1D_{NC'}$, and $^2D_{HNC'}$) in two different alignment media (pf1 phage and polyethylene glycol/hexanol). RDCs provide orientational restraints relative to an external alignment tensor (28), and the two alignment media provide complementary information, because their alignment tensors are significantly different from one another with a normalized scalar product of 0.57. A summary of the structural statistics is provided in Table 1, and a stereoview of a best-fit superposition of the backbone atoms of the 130 final simulated annealing structures is shown in Fig. 1*A*. Residues 157–159 at the N terminus and 322–323 at the C terminus are disordered. The rest of the structure (residues 160–321) is well defined with a backbone (N, Cα, C′, and O) precision of 0.26 ± 0.04 Å. 93% of the residues occupy the most favorable region of Ramachandran space (48) and the hydrogen bonding data base potential (43) automatically identified 93 backbone hydrogen bonds (of which only 55 were explicitly identified based on the pattern of NOEs).

The structure of IIB^{Man} comprises a central seven-stranded mixed β-sheet (β1, β2, β3, β4, β5, β8, and β9) with a [$-2x$, $-1x$, $2x$, $2x$, $1x$, 1] topology, surrounded by seven α-helices and a short antiparallel β-sheet (β6 and β7). The active site (residues 172–176) immediately precedes helix α1. The side chain of the active site His-175 is in a g^+/g^+ conformation stabilized by an electrostatic interaction between the carboxylate of Asp-170 and its Nϵ2-H atom, with the Nδ1 atom exposed to solvent and available for phosphorylation.

Not surprisingly the solution NMR structure of *E. coli* IIB^{Man} is similar to that of the x-ray structures of *K. pneumoniae* IIB^{Sor} (2.9-Å resolution) (49) and *B. subtilis* IIB^{Lev} (1.75-Å resolution) (50), as expected from their high percentage sequence identity (42 and 49%, respectively). The Cα backbone r.m.s. differences are 1.0 and 1.4 Å, respectively, for the complete polypeptide chain, and 1.1 and 0.7 Å, respectively, for residues 163–186 comprising strand β1 (163–170), the active site loop (residues 171–176), and helix α1 (residues 177–186).

Binding of IIA^{Man} to IIB^{Man}—Three-dimensional ^{12}C-filtered/^{13}C-separated NOE experiments carried out on complexes of wild-type IIA^{Man} with IIB^{Man} revealed a pattern of intermolecular NOEs that was not consistent with a single spe-

mination of the IIA^{Man}-IIB^{Man} complex was carried out using conjoined rigid body/torsion angle dynamics (21, 37). The target function for simulated annealing comprises the following: square well potentials for interproton distance and torsion angle restraints (38); harmonic potentials for ^{13}Cα/^{13}Cβ chemical shift restraints (39), RDC restraints (40), and covalent geometry; and a quartic van der Waals repulsion potential (41), a multidimensional torsion angle data base potential of mean force (42), a backbone hydrogen bonding data base potential of mean force with automatic hydrogen-bond selection (43), and a gyration volume term (44) to represent the non-bonded contacts. The gyration volume term represents a general, weak overall packing potential for any ellipsoidal-shaped molecule based on the observation that proteins pack to a constant density (45). Structures were displayed using VMD-XPLOR (46) and GRASP (47).

RESULTS AND DISCUSSION

Structure of IIB^{Man}—The solution structure of IIB^{Man} was solved on the basis of 3091 experimental NMR restraints,

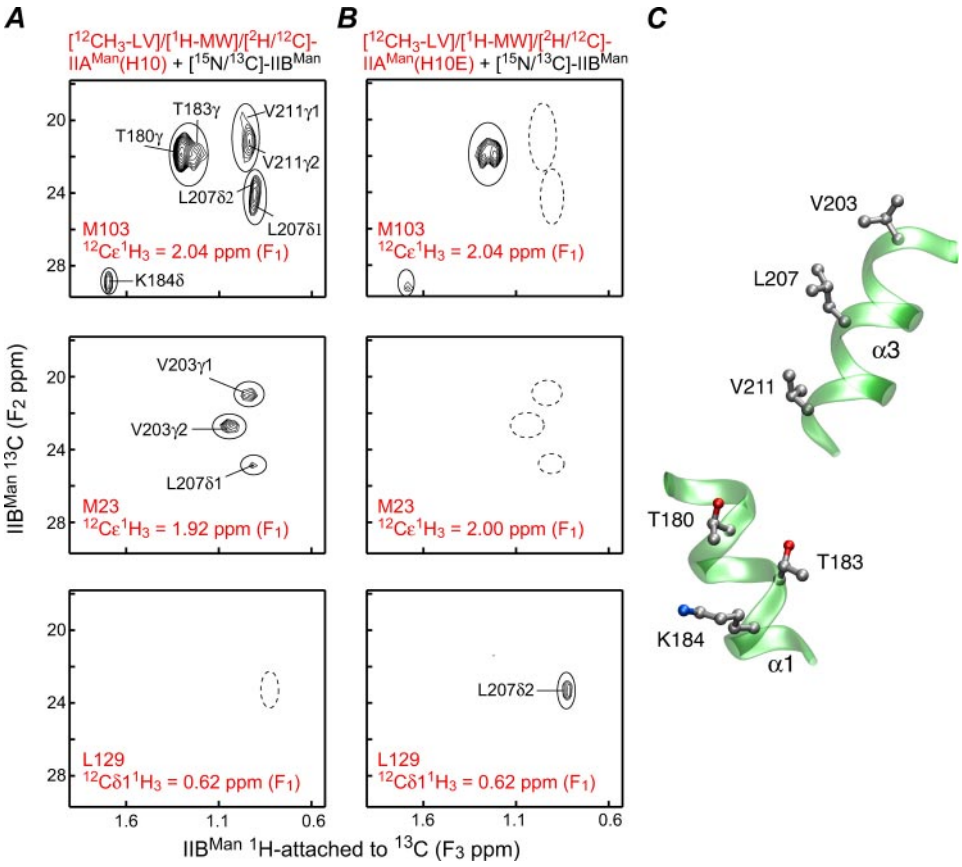

FIGURE 2. **Intermolecular NOEs observed in the IIA^{Man}-IIB^{Man} complex.** Methyl region of ^{1}H(^{13}C-attached, F$_3$)/^{13}C(F$_2$) planes from a three-dimensional ^{12}C-filtered(F$_1$)/^{13}C-separated(F$_2$) NOE-HSQC spectrum displaying NOEs from the methyl protons of Met-103 (*top panels*), Met-23 (*middle panels*), and Leu-129 δ1 (*bottom panels*) of [^{12}CH$_3$-LV]/[^{1}H-MV]/[^{2}H/^{12}C/^{14}N]-IIA^{Man} to protons attached to ^{13}C of [U-^{15}N/^{13}C]-IIB^{Man}. *A*, wild-type IIA^{Man}(H10) and IIB^{Man}. *B*, IIA^{Man}(H10E) and IIB^{Man}. *C*, location of the two clusters of residues located on helices α1 and α3 of IIB^{Man} that are far apart in the structure but exhibit NOEs to the methyl group of Met-103 in the wild-type sample. The wild-type sample (*A*) displays NOEs arising from a mixture of two complexes comprising one that is compatible with phosphoryl transfer (productive) and the other where phosphoryl transfer cannot take place (non-productive); the complex of the phosphomimetic IIA^{Man}(H10E) with IIB^{Man} (*B*) corresponds to a single productive complex.

cies and suggested the presence of two co-existing complexes (Fig. 2). This is best illustrated by the *top panel* in Fig. 2*A*, which shows intermolecular NOEs from the isolated resonance of the methyl group of Met-103 of [^{12}CH$_3$-LV]/[^{1}H-MW]/[^{12}C/^{14}N/^{2}H]-IIA^{Man} to the methyl group region of [U-^{13}C/^{15}N]-IIB^{Man}. NOEs are observed to the methyl groups of Leu-207 and Val-211, which form one cluster on the surface of IIB^{Man}, and to the methyl groups of Thr-180 and Thr-183, as well as the δ-methylene group of Lys-184, which form a second cluster. Because the methyl groups of Val-211/Leu-207 are ~11/18, ~13/19, and ~16/22 Å away from the methyl groups of Thr-180 and Thr-183 and the δ-methylene group of Lys-184, respectively, it is evident that the methyl group of Met-103 of IIA^{Man} cannot be close to both clusters of residues simultaneously (Fig. 2*C*).

Further qualitative interpretation of the intermolecular NOE data suggested that a small number of NOEs were consistent with a productive complex, that is one in which the two active site histidines, His-10 of IIA^{Man} and His-175 of IIB^{Man}, are in close proximity and therefore capable of phosphoryl transfer, whereas the majority of NOEs arose from a non-productive complex. However, in the absence of prior detailed knowledge of one or the other structure, resolving the structures of two complexes simultaneously from the data was not feasible.

We reasoned that a possible explanation for the existence of two complexes could involve the conserved, solvent-exposed Arg-172 in close proximity to the active site His-175 of IIB^{Man}. In the productive complex, Arg-172 would be buried at the interface and had been previously postulated to interact with the negatively charged phosphoryl group on His-10 of IIA^{Man} (50). In the absence of histidine phosphorylation burial of the positively charged guanidinium group of Arg-172 at a protein-protein interface is likely to disfavor the formation of the productive complex. To test this hypothesis we mutated His-10 of IIA^{Man} to Glu to mimic the effect of phosphorylation of His-10 (at its Nε2 position). Analysis of the intermolecular NOE data for the resulting complex of the IIA^{Man}(H10E) mutant with IIB^{Man} was fully consistent with the formation of a single complex corresponding to the productive phosphoryl transfer complex. The change in the pattern of observed intermolecular NOEs can be seen by comparison of Figs. 2*A* and *B*.

Both wild-type and H10E IIA^{Man} bind weakly to IIB^{Man}, and the complexes are in fast exchange on the chemical shift time scale. The change in pattern of intermolecular NOEs between the complex of wild-type and H10E IIA^{Man} with IIB^{Man} is accompanied by differences in the chemical shift perturbation of methyl groups of IIB^{Man} observed upon titration (Fig. 3*A*). Interestingly, the apparent affinity of the complex of IIB^{Man} with both wild-type IIA^{Man} and the H10E mutant are very comparable with an equilibrium dissociation constant (K_D) of ~0.5 mM (Fig. 3*B*). Although binding is weak, in the context of intact IIAB^{Man}, where the A and B domains are connected by a flexible 25-residue linker, one can calculate (11, 51), based upon the expected average end-to-end distance of ~50 Å for the linker (52), that there would be an ~85% probability of the two domains interacting with one another at any given time.

Structure Determination of the Productive and Non-productive IIA^{Man}-IIB^{Man} Complexes—The NMR samples used for structure determination comprised a mixture of 1 equivalent IIA^{Man} dimer to 1 equivalent IIB^{Man} monomer. IIA^{Man} is a symmetric dimer, and the final stoichiometry of both the productive and non-productive complexes is 1 equivalent of IIA^{Man} dimer to 2 equivalents of IIB^{Man}. The use of a 1:1 mixture was

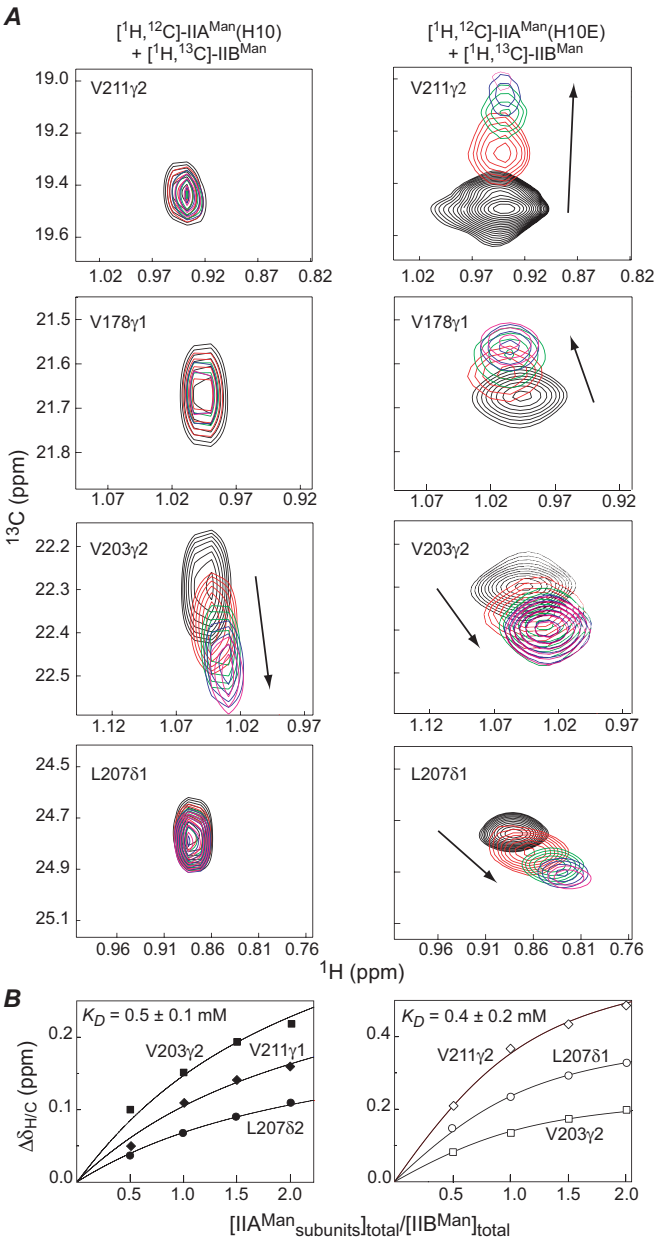

FIGURE 3. **Binding of IIB^{Man} to wild-type IIA^{Man} (*left-hand panels*) and the phosphomimetic H10E mutant of IIA^{Man} (*right-hand panels*).** *A*, contour plots of isolated methyl group resonances of IIB^{Man} obtained from two-dimensional constant-time ^{1}H-^{13}C HMQC spectra recorded at [IIA^{Man}]$_{subunits}$/[IIB^{Man}]$_{total}$ ratios of 0 (*black*), 0.5 (*red*), 1.0 (*green*), 1.5 (*blue*), and 2.0 (*magenta*). *B*, chemical shift perturbation ($\Delta\delta_{H/C} = [25\Delta\delta(^1H)^2 + \Delta\delta(^{13}C)^2]^{1/2}$ of selected methyl groups of IIB^{Man} as a function of added IIA^{Man}. The *symbols* represent the experimental data, and the *solid continuous lines* are global best-fit theoretical curves for a simple binding isotherm. The concentration of IIA^{Man} is expressed on a subunit basis (*i.e.* two IIB^{Man} binding sites per IIA^{Man} dimer).

chosen to optimize the line widths of both components, IIA^{Man} and IIB^{Man}, simultaneously. Because binding is weak, the samples will always comprise a mixture of free, 1:1 and 1:2 complexes in fast exchange with one another at the concentrations employed in the NMR experiments (0.5–1 mM). The line widths are proportional to the population average molecular weights. Given a K_D of ~0.5 mM, a sample containing 1 mM IIA^{Man} dimer and 1 mM IIB^{Man} (with free molecular masses of 35 and 19 kDa, respectively), will comprise ~59 and ~72% complexed IIA^{Man} and IIB^{Man}, respectively, with an apparent molecular mass of ~49 kDa for both IIA^{Man} and IIB^{Man}. In contrast, a mixture of 1 mM IIA^{Man} and 2 mM IIB^{Man} will yield an effective molecular mass of 58 kDa for IIA^{Man} and 48 kDa for IIB^{Man}.

We first solved the structure of the productive complex using data exclusively from the IIA^{Man}(H10E)-IIB^{Man} samples. The changes in ^{1}H/^{15}N shifts upon complexation are very small indicating no significant structural perturbation in the backbone coordinates of either IIA^{Man} or IIB^{Man} occurs upon binding (at the level of detection of the NMR data). We therefore solved the structure of the productive complex using a hybrid approach that employs conjoined rigid body/torsion angle dynamics (20, 21) on the basis of intermolecular NOE data with the coordinates of free IIA^{Man} (x-ray, PDB code 1POD) (16) and IIB^{Man} (the complete ensemble of NMR simulated annealing structures; this report) treated as rigid bodies and the interfacial side chains given torsional degrees of freedom. In addition, the backbone and side chains of residues 130–134 of IIA^{Man} were also given torsional degrees of freedom, because intermolecular NOEs were observed involving residues 129, 133, and 134, although residues 131–133 were not visible in the electron density map of the free crystal structure (16). 37 intermolecular NOEs were identified of which 33 are between unique proton pairs, and the remaining 4 are ambiguous involving potentially alternate partners and were therefore treated as $(\Sigma r^{-6})^{-1/6}$ sums. The active site His-10 is located right at the interface of the two identical subunits of IIA^{Man}. Because the Cα atom positions of the two symmetrically related active site histidines, His-10 and His-10′, are separated by 20 Å, there is no issue attributing the intermolecular NOEs to one or other subunit of IIA^{Man}. It should be noted that the use of RDCs to provide orientational information for the structure determination of the complex was precluded owing to uncertainties in the exact proportions of each component in the sample (*i.e.* free proteins, complex with one IIB^{Man} bound and complex with two IIB^{Man} molecules bound, all of which will have different alignment tensors), and the unfeasibility of deconvoluting the alignment tensors of the 1:1 and 1:2 complexes (because complete occupancy of the 1:2 complex cannot be achieved at concentrations compatible with the alignment media used for RDC measurements). A summary of the structural statistics is given in Table 2, and a best-fit superposition of the final 120 simulated annealing structures is shown in Fig. 4*A*. The relative orientation of IIB^{Man} relative to the IIA^{Man} dimer is well determined by the intermolecular NOE data with an overall backbone precision for the complex of 0.5 Å.

As noted above, samples of wild-type IIA^{Man} and IIB^{Man} comprise a mixture of productive and non-productive complexes. Of the 41 intermolecular NOEs identified, only 5 satisfied the structure of the productive complex with violations < 0.5 Å, and the remainder are violated by 4–16 Å. To obtain the structure of the non-productive complex, we therefore proceeded as follows. The structure of the productive complex (restrained regularized mean coordinates) was held fixed and a second molecule of IIB^{Man} (restrained regularized mean structure of free IIB^{Man}) was introduced in random starting orientations and its position determined by conjoined rigid body/torsion angle dynamics (21) with the assigned intermo-

TABLE 2

Structural statistics for productive and non-productive IIA^{Man}-IIB^{Man} complexes

The notation is the same as that in Table 1. The final number of simulated annealing structures is 120. The number of experimental restraints for the various terms is given in parentheses, with the first number referring to the data for the productive complex derived from the IIA^{Man}(H10E)-IIB^{Man} complex, and the second to the data from the wild type IIA^{Man}(H10)-IIB^{Man} complex.

	Productive complex		Non-productive complex	
	⟨SA⟩	(SA)$_r$	⟨SA⟩	(SA)$_r$
r.m.s. deviations from experimental restraints[a]				
Intermolecular interproton distances (Å) (37/41[b])	0.02 ± 0.01	0	0.02 ± 0.01	0.05
Side-chain torsion angles (°) (47/30)[c]	0.60 ± 0.07	0.72	0.66 ± 0.06	1.17
Measures of structure quality[d]				
Intermolecular repulsion energy (kcal.mol^{-1})	2.9 + 1.5	7.7	0.1 ± 0.1	0.5
Intermolecular Lennard-Jones energy (kcal.mol^{-1})	−28.1 ± 4.9	−30.4	−10.5 ± 2.4	−11.1
Coordinate precision of the complex (Å)[e]				
Complete backbone (N, Cα, C′, and O) atoms	0.52 ± 0.15		0.76 ± 0.28	
Interfacial side-chain heavy atoms	1.30 ± 0.10		1.26 ± 0.17	

[a] None of the structures exhibit NOE distance violations >0.3 Å or torsion angle violations >5°.

[b] The data obtained for the wild-type IIA^{Man}(H10E)-IIB^{Man} complex arise from a mixture of productive and unproductive complexes. The NOE data were therefore represented as ambiguous $(\Sigma r^{-6})^{-1/6}$ sums. The productive complex was held fixed at the conformation determined from the IIA^{Man}(H10E)-IIB^{Man} data. Of the 41 intermolecular NOEs, only 5 (attributable to the productive complex) are not satisfied (*i.e.* violations > 0.5 Å) by the non-productive complex alone.

[c] For the productive complex, the side-chain torsion angles comprise 11 χ_1 and 5 χ_2 for IIA^{Man}, and 14 χ_1 and 7 χ_2 for IIB^{Man}; in addition, there are 4ϕ and 3 ψ backbone torsion angle restraints for residues 130–134 of IIA^{Man}, which were also given torsional degrees of freedom. For the non-productive complex, the side-chain torsion angles comprise 11 χ_1 and 5 χ_2 for IIA^{Man}, and 5 χ_1 and 1 χ_2 for IIB^{Man}.

[d] The intermolecular repulsion energy is given by the value of the quartic van der Waals repulsion term calculated with a force constant of 4 kcal.mol^{-1}.Å^{-4} and a van der Waals radius scale factor of 0.78. The intermolecular Lennard-Jones van der Waals interaction energy is calculated using the CHARMM19/20 parameters and is not included in the target function used to calculate the structures. The percentage of residues present in the most favorable region of the Ramachandran map (48) for the x-ray structure of free IIA^{Man} (PDB code 1PDO (16)) is 93.3%.

[e] Defined as the average r.m.s. difference between the final 120 conjoined rigid body/torsion angle dynamics simulated annealing structures and the mean coordinate positions. The values quoted for the complete backbone indicate the precision with which the orientation and translation of the IIA^{Man} dimer and IIB^{Man} have been determined relative to one another. Because the backbone of IIA^{Man} is treated as a rigid body, the backbone values do not take into account the error in the x-ray coordinates of IIA^{Man} (estimated at <0.3 Å). For the productive H10E(IIA^{Man})-IIB^{Man} complex, the values for the backbone do take into account the precision of the free IIB^{Man} coordinates, although the backbone of IIB^{Man} is treated as a rigid body, because the complete ensemble of simulated annealing structures for IIB^{Man} was employed in the calculations. For the non-productive complex the value for the backbone does not take into account the precision of the IIB^{Man} coordinates, because the calculations used the restrained regularized mean coordinates of IIB^{Man}.

lecular NOEs represented as ambiguous restraints, that is $(\Sigma r^{-6})^{-1/6}$ sums (34), arising from both the productive and non-productive complexes. (Note that because the intermolecular NOEs are interpreted in terms of loose, conservative distance ranges, and because long distances do not contribute to the $(\Sigma r^{-6})^{-1/6}$ sum, it is not necessary to know the proportion of productive and non-productive complexes present in the sample). A table of structural statistics is provided in Table 2, and a best-fit superposition of the ensemble of 120 simulated annealing structures of the non-productive complex is displayed in Fig. 4*B*. Although the relative orientation of IIB^{Man} relative to IIA^{Man} is not quite as well defined in the non-productive complex relative to the productive one, the backbone precision for the non-productive complex is still rather high (~0.8 Å). It is worth noting that the same ensemble of structures was obtained for the non-productive complex by simply using the 36 intermolecular NOEs that were violated in the productive complex and not including the structure of the productive complex in the calculations.

Structure of the Productive IIA^{Man}-IIB^{Man} Complex—A ribbon diagram of the productive complex derived from the IIA^{Man}(H10E)-IIB^{Man} data is shown in Fig. 5*A*. 1750 Å^2 of solvent-accessible surface area is buried at the interface, 870 Å^2 originating from IIA^{Man} and 880 Å^2 from IIB^{Man}. The dimensions of the interface are ~40 Å long and 30 Å wide. The gap volume index (ratio of gap volume to buried accessible surface area) is 3.5, which falls in the outer range observed for both hetero (2.4 ± 1.0) and optional (2.7 ± 0.9) protein-protein complexes (53), as expected given the weak binding.

In describing the intermolecular contacts involving IIA^{Man}, the residues of the B-chain (*red subunit* in Figs. 5–8) are denoted by a prime symbol. (Note that the definition of A and B chains of IIA^{Man} is purely arbitrary, and the relationship of the two IIA^{Man} chains to IIB^{Man} at one site is reversed in the symmetry related site.)

The interface on IIA^{Man} is made up of residues of both subunits and comprises helix α1, helix α4, and the C-terminal five residues of the A-chain: the active site His-10′, the loop between β2′ and α2′, the N-terminal end of helix α2′, and helix α3′ of the B-chain. The interface on IIB^{Man} comprises the active site (residues 172–176, including His-175), helices α1 and α3, and the loops between strands β5 and β6, β6 and β7, and β8 and β9 (Fig. 5, *A* and *C*). A summary of the contacts is provided in Fig. 5*C*, and a stereoview showing the side-chain interactions is shown in Fig. 6*A*. The A chain of IIA^{Man} primarily interacts with helices α1 and α3, and the loop between strands β8 and β9 of IIB^{Man}, whereas the B-chain primarily contacts the active site loop, helix α3, and the loops between strands β5 and β6 and strands β6 and β7 of IIB^{Man}.

The interface is made up of 57% non-polar atoms and 43% polar ones. The active site histidines, His-10′ and His-175, are located at the center of the interface, as is Arg-172. In the IIA^{Man}(H10E)-IIB^{Man} complex, the positively charged guanidino group of Arg-172 is neutralized by the negative charge on the carboxylate of H10E′, mimicking phosphorylated His-10′. In the absence of neutralization of the guanidino group of Arg-172, the productive complex is destabilized allowing an alternative, non-productive complex to be formed. The majority of intermolecular interactions are hydrophobic in nature, and there are only three additional electrostatic interactions, between Asp-106 and Arg-180, and Glu-100 and Lys-184, which anchor helix α1 of IIB^{Man}, and between Glu-43′ and Arg-

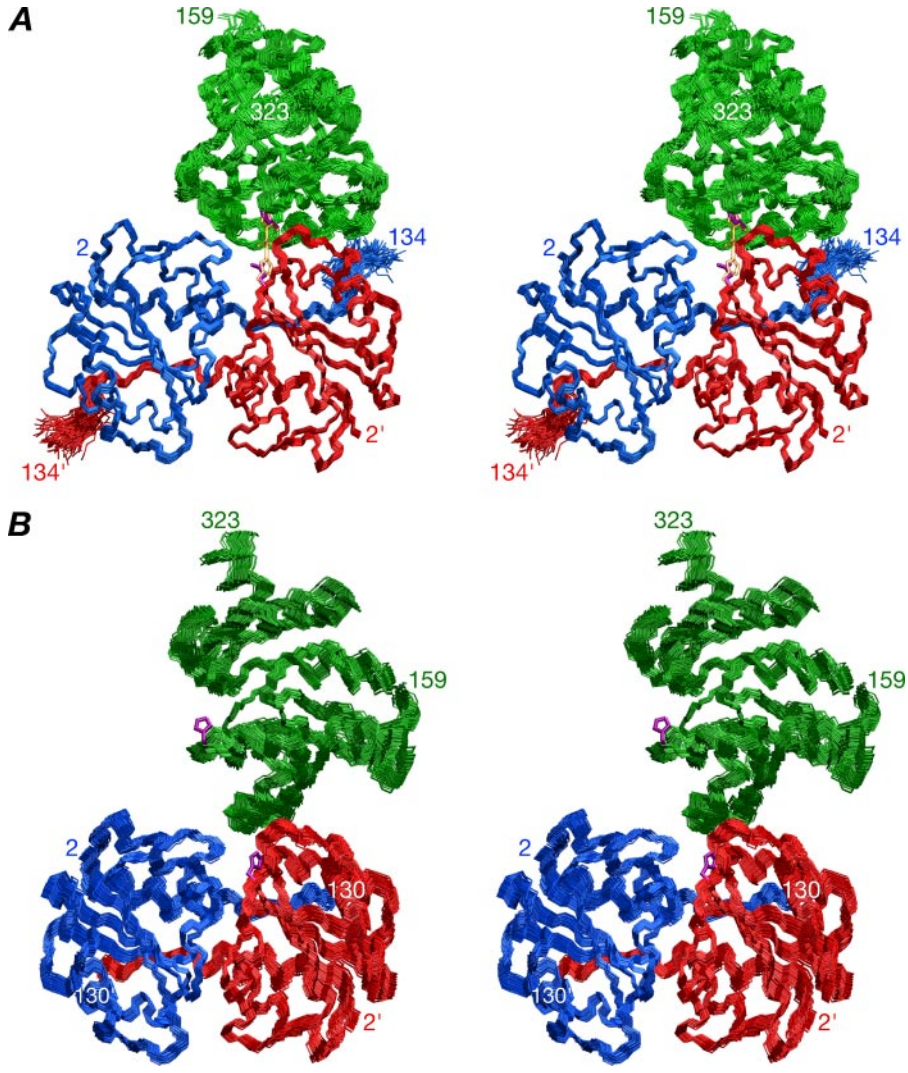

FIGURE 4. **Structures of the productive and non-productive IIA^{Man}-IIB^{Man} complexes in solution.** Stereo-views showing best-fit superpositions of backbone (N, Cα, and C) atoms for the final 120 simulated annealing structures, with IIB^{Man} in *green*, and the A and B subunits of IIA^{Man} in *blue* and *red*, respectively; the active site side chains of the restrained regularized mean structure are shown in *purple*. *A*, structure corresponding to the productive, phosphoryl transfer competent complex, derived from the NOE data obtained with the phosphomimetic H10E mutant of IIA^{Man}. The modeled phosphoryl transition state with a pentacoordinate phosphoryl group and Glu-10 replaced by His is shown in *transparent orange*. Only negligible changes (<0.2 Å) in local backbone conformation in the immediate vicinity of the active sites (residues 8′–12′ and 173–177) are required to model the phosphoryl transition state. *B*, structure corresponding to the non-productive, phosphoryl transfer incompetent, complex derived from the NOE data obtained with wild-type IIA^{Man}. The Cα–Cα distance between the active site residues (residue 10′ of the B chain of IIA^{Man} and residue 175 of IIB^{Man}) is 11 Å for the productive complex *versus* 25 Å for the non-productive one.

271, which anchors the loop between strands β5 and β6 of IIB^{Man}. A ridge of hydrophobic residues comprising Met-23, Leu-24, Leu-25, Val-99, and Met-103 of IIA^{Man} provide non-polar interactions with complementary residues on helix α1 and the loop between strands β8 and β9 of IIB^{Man}. Thr-202, Val-203, Leu-207, and Val-211 of helix α3 of IIB^{Man} are wedged in a hydrophobic groove formed by Leu-129, Lys-132, Pro-133, and Val-134 of the C terminus of the A-chain of IIA^{Man} and Trp-69′ of the B chain of IIA^{Man}.

Phosphoryl transfer between IIA^{Man} and IIB^{Man}, as in other PTS complexes, is known to proceed through a transition state involving a pentacoordinate phosphoryl group in a trigonal bipyramidal geometry with the donor (Nϵ2 of His-10′ of IIA^{Man}) and acceptor (Nδ1 of His-175 of IIB^{Man}) atoms in apical positions (54, 55). The transition state can readily be modeled on the basis of the structure of the IIA^{Man}(H10E)-IIB^{Man} complex using the procedures described previously (6–9) in which the only portion of the complex allowed to move comprises the backbone and side chains of the active site histidines (His-10′ and His-175), the immediately adjacent residues (residues 8–12′ of IIA^{Man} and 173–177 of IIB^{Man}) and the phosphoryl group (Figs. 4*A* and 6*B*). For an N–P distance of 2.5 Å, which corresponds to a mechanism with substantial dissociative character consistent with many phosphoryl transfer reactions (56), the transition state can be accommodated with negligible (<0.2 Å) changes in backbone conformation for residues 9′–11′ and 174–176. Only minor additional backbone changes (~0.2 Å) for these residues are required for an S_N2 mechanism (50% associative) with an N–P distance of 2 Å.

The His-10′–P–His-175 transition state is buried within a largely hydrophobic cavity comprising Leu-24, Phe-36′, Pro-38′, and Pro-73′ of IIA^{Man}, and Val-178 and the aliphatic portions of the long side chains of Arg-172 and Lys-305 of IIB^{Man}. The phosphoryl group is within hydrogen bonding distance of the hydroxyl group of Ser-72′ and the guanidino group of Arg-172, thereby stabilizing the transition state. In addition, there may be water-bridged interactions to the phosphoryl group from the hydroxyl group of Thr-68′, the carboxyamide of Gln-177, and the NH_3 group of Lys-305 (Fig. 6, *B* and *C*).

The Cα–Cα distances between the N terminus of IIB^{Man} (residue 209) and the C termini (residues 134 and 134′) of the A and B chains of IIA^{Man} are 38 Å and 64 Å, respectively. The expected average end-to-end distance for a random-coil 25-residue linker is ~50 Å (52). This suggests that, in the intact IIAB^{Man} dimer, phosphoryl transfer occurs predominantly in *trans*, that is between the IIA^{Man} domain of one chain, and the IIB^{Man} domain of the other chain.

The structure of the productive IIA^{Man}-IIB^{Man} complex displays both similarities and differences to the structure of the upstream IIA^{Man}-HPr complex (9). Both IIB^{Man} and HPr have an active site loop followed by an α-helix. The Cα atomic r.m.s. difference between the element of structure

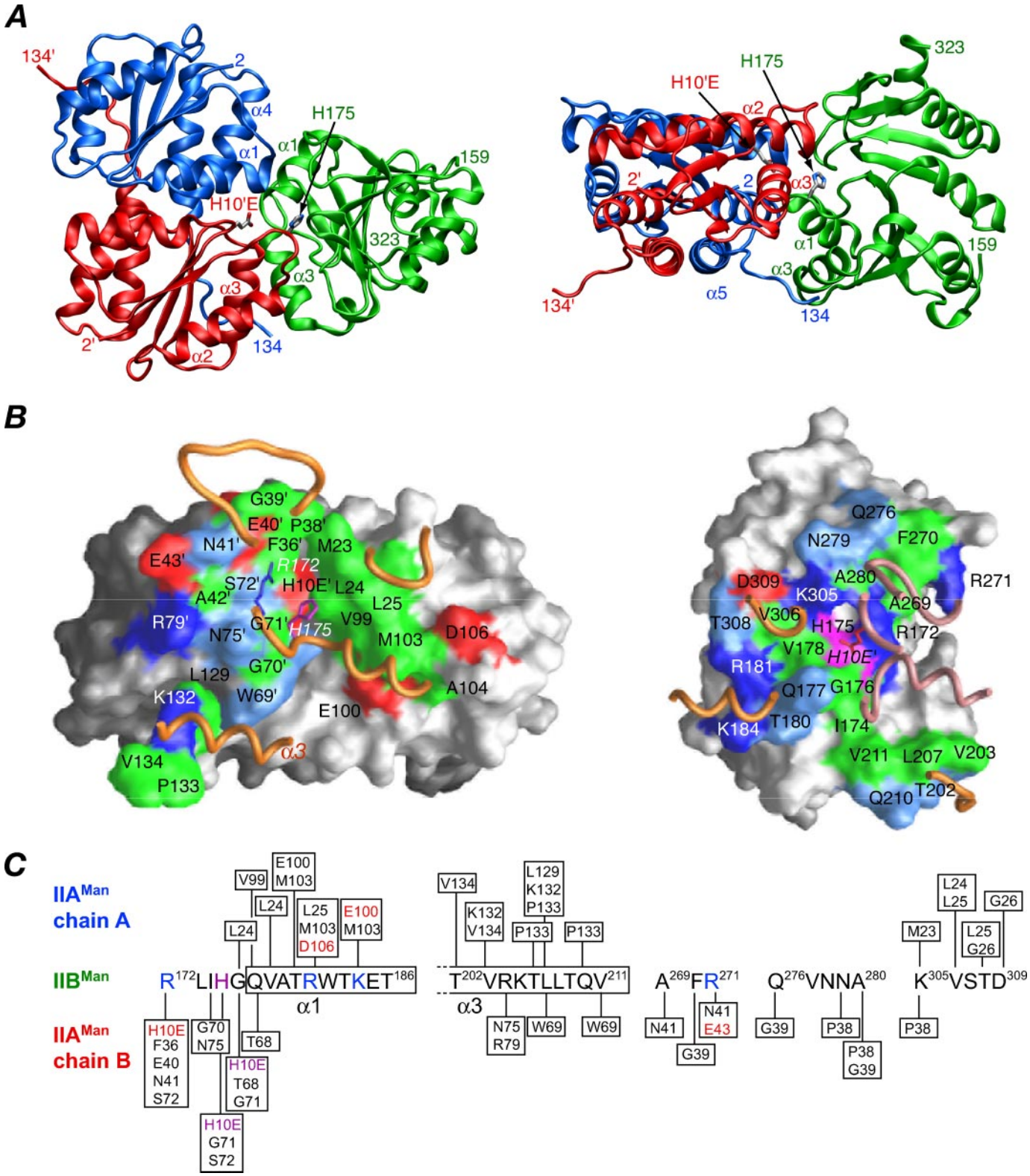

FIGURE 5. **Overall view of the productive, phosphomimetic IIA^{Man}(H10E)-IIB^{Man} complex.** *A*, ribbon diagram with the A and B chains of IIA^{Man} in *blue* and *red*, respectively, and IIB^{Man} in *green*; the active site residues H10E′ of IIA^{Man} (chain B) and H175 of IIB^{Man} are also displayed. *B*, interaction surfaces for the productive IIA^{Man}(H10E)-IIB^{Man} complex. The *left* and *right panels* display the interaction surfaces on IIA^{Man} and IIB^{Man}, respectively. The surfaces are color coded as follows: hydrophobic residues are *green*, uncharged residues bearing a polar functional group are *cyan*, negatively charged residues are *red*, positively charged residues are *blue*, active site histidines are *purple*, and non-interfacial residues are *gray* (with a *darker shade* for the B subunit of IIA^{Man}). Relevant portions of the backbone of the interacting partner are displayed as *tubes* (IIB^{Man} in *gold*, A chain of IIA^{Man} in *gold*, and B chain of IIA^{Man} in *lilac*). The side chains of His-175 and Arg-172 of IIB^{Man} are shown in the *left-hand panel*, and the side chain of H10E′ of the B chain of IIA^{Man} is displayed in the *right-hand panel* (labeled in *italics*). *C*, diagrammatic representation of the intermolecular contacts with the active site histidines colored in *purple*, and residues involved in potential side chain-side chain intermolecular electrostatic interactions colored in *red* (acceptor) and *blue* (donor).

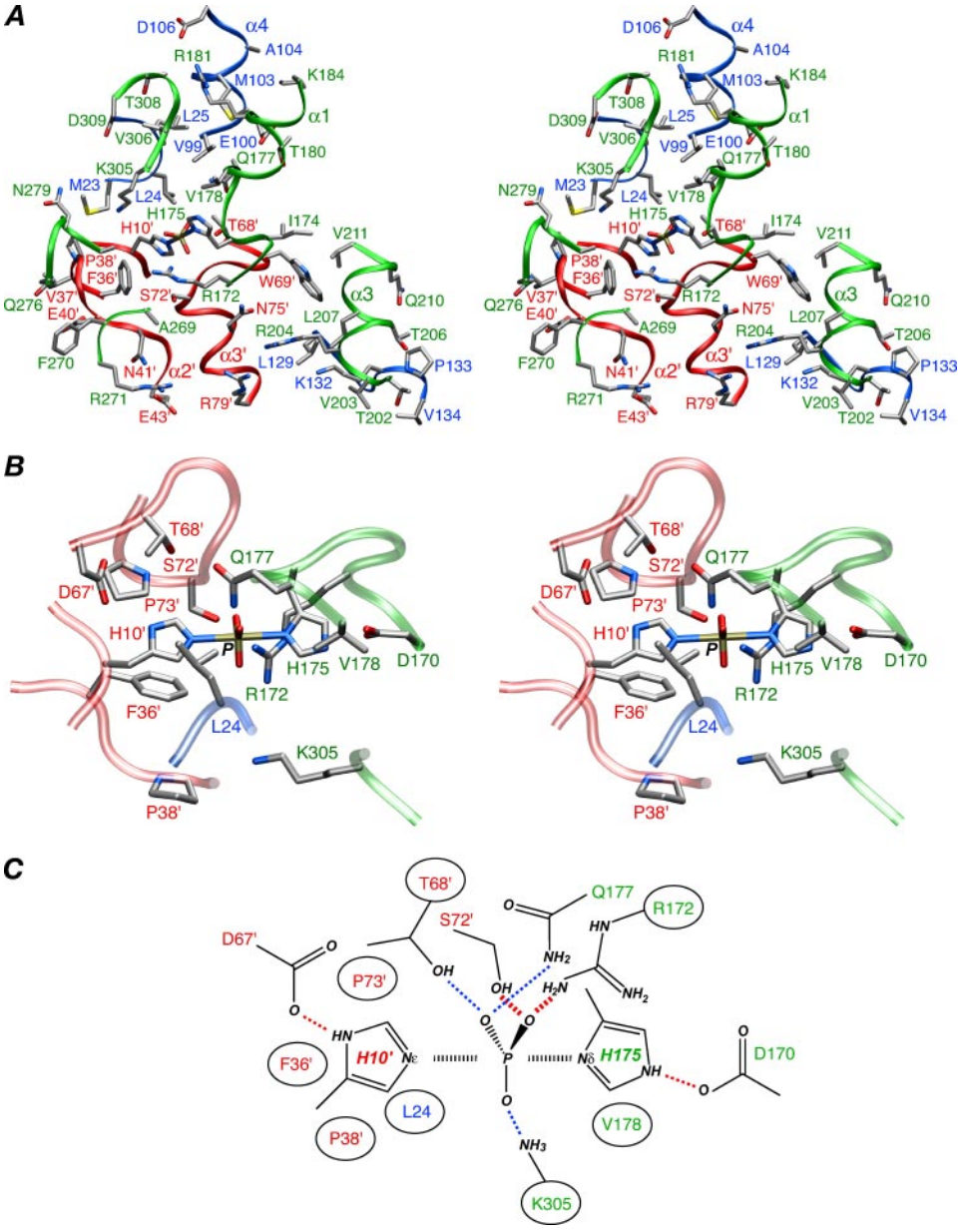

FIGURE 6. **The IIA^{Man}(H10E)-IIB^{Man} interface and the phosphoryl transition state.** *A*, overall stereoview of the interface, including the modeled His-10′—P—His-175 phosphoryl transition state. *B*, enlarged view depicting the vicinity around the His-10′—P—His-175 transition state. *C*, schematic diagram of the phosphoryl transition state. In *A* and *B*, the backbones are depicted as *ribbons* (*blue*, chain A of IIA^{Man}; *red*, chain B of IIA^{Man}; and *green*, IIB^{Man}), and the side-chain atoms are colored according to atom type; carbon, *gray*; nitrogen, *blue*; oxygen, *red*; sulfur, *yellow*, phosphorus, *tan*. In *C*, *red dashed lines* indicate likely hydrogen bonds with donor acceptor distances < 3.5 Å; *blue dashed lines* represent potential water-bridged interactions with donor-acceptor distances between 5 and 6 Å. The phosphorus and active site histidines are surrounded by a large number of hydrophobic residues (*circled*), including the long aliphatic side chains of Arg-172 and Lys-305 of IIB^{Man}.

form by the active site loop and helix α1 (residues 171–186 of IIB^{Man} and 11–26 of HPr) in the two structures is 1.7 Å. A comparison of the structures of the IIA^{Man}-IIB^{Man} and IIA^{Man}-HPr complexes, superimposed on the coordinates of IIA^{Man}, is shown in Fig. 7. The similar disposition of the active site loop and helix α1 of IIB^{Man} and HPr relative to IIA^{Man} is evident. However, the interface is more extensive in the IIA^{Man}-IIB^{Man} complex than in the IIA^{Man}-HPr complex (1750 Å^2 buried *versus* 1450 Å^2). Moreover, HPr has a large contact surface with the A chain of IIA^{Man}, whereas IIB^{Man} has more extensive contacts with the B chain. Despite the reduced contact area, the affinity of HPr for IIA^{Man} ($K_D \sim 30$ μM 9) is 15- to 20-fold higher than that of IIB^{Man} ($K_D \sim 0.5$ mM; this report). This may be due to a higher degree of surface complementary, as exemplified, for example, by a 2-fold greater number of electrostatic/hydrogen-bonding interactions between HPr and IIA^{Man} (9).

Structure of the Non-productive IIA^{Man}-IIB^{Man} Complex—A ribbon diagram of the non-productive complex is shown in Fig. 8*A*. The interaction involves a highly hydrophobic ridge-like protrusion on the surface of IIB^{Man} formed exclusively by helix α3, interacting with a subset of residues on IIA^{Man} that comprise the central portion of the interface involved in the productive complex (Fig. 8*C*). This subset comprises the predominantly hydrophobic surface formed by helices α1 (Met-23, Leu-24, and Leu-25) and α4 (Pro-96, Val-99, and Met-103) of the A-chain of IIA^{Man}, and the active site His-10′, the loop following strand β2′ (Phe-36′), the loop between strand β3′ and helix α3′ (Thr-68′, Trp-69′, and Gly-70′), and helix α3′ (Ser-72′ and Asn-75′) of the B chain of IIA^{Man} (Fig. 8, *B* and *C*). The buried accessible surface area at the interface is 790 Å^2, of which 380 Å^2 originates from IIA^{Man} and 410 Å^2 from IIB^{Man}, approximately half that of the productive complex. The Cα–Cα distance between the two active site histidines, His-10′ and His-175, is 25 Å and therefore incompatible with phosphoryl transfer between IIA^{Man} and IIB^{Man}. The Cα–Cα distances between the N terminus of IIB^{Man} and the C termini of the A and B chains of IIA^{Man} are 60 and 30 Å, respectively (Fig. 8*A*). Thus, just as in the case of the productive complex, the interaction between the IIB^{Man} domain and IIA^{Man} domain is likely to occur in *trans* in the intact IIAB^{Man} dimer.

The orientation of IIB^{Man} relative to IIA^{Man} in the non-productive complex is related by a ~90-Å rotation and ~37-Å translation relative to the productive one. This is readily appreciated from a comparison of the location of helix α3 of IIB^{Man} on the surface of IIA^{Man} in the two complexes provided by Figs. 5*B* and 8*C* (*left-hand panels*).

The active site of IIB^{Man}, including His-175 and Arg-172, is fully exposed to solvent in the non-productive complex, and

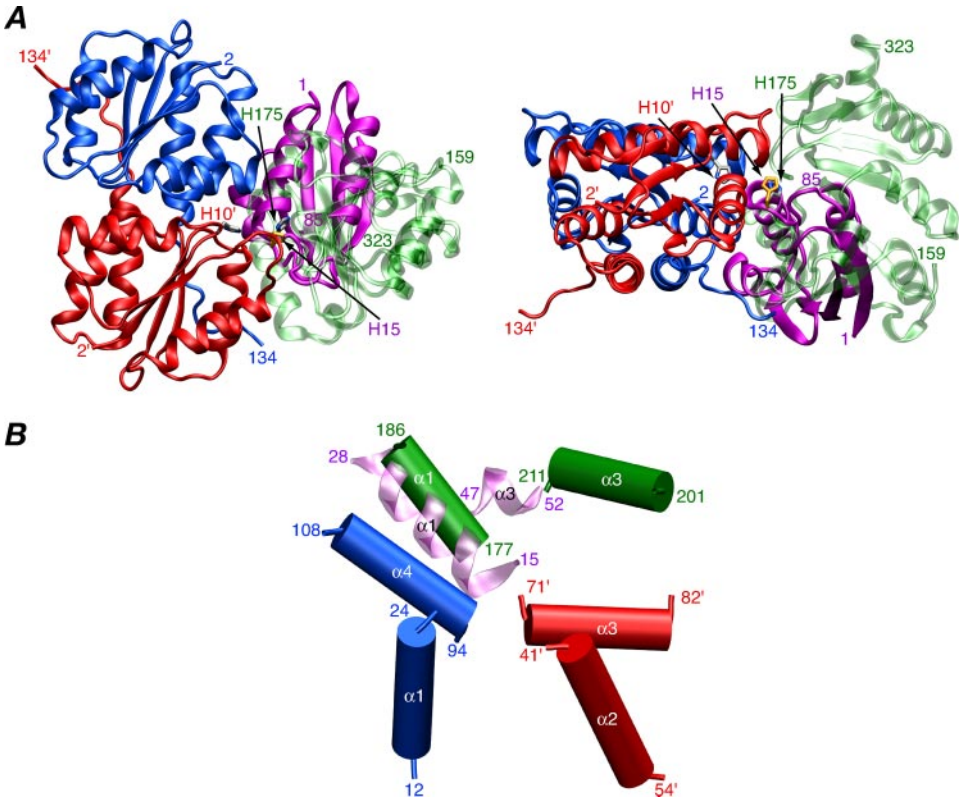

FIGURE 7. **Comparison of the IIA^{Man}-HPr complex with the productive IIA^{Man}-IIB^{Man} complex.** *A*, ribbon diagram showing a comparison of the IIA^{Man}-HPr (PDB code 1VRC (9)) and IIA^{Man}-IIB^{Man} complexes superimposed on the coordinates of IIA^{Man}. The A and B subunits of IIA^{Man} are shown in *blue* and *red*, respectively, HPr is shown in *purple*, and IIB^{Man} is in *transparent green*. The active site residues are also displayed (His-10′ of the B chain of IIA^{Man}, His-15 of HPr, and His-175 of IIB^{Man}). *B*, comparison of intermolecular helical-helical interactions in the IIA^{Man}-IIB^{Man} and IIA^{Man}-HPr complexes, helices α1 and α3 of IIB^{Man} in *green*, helices α1 and α3 of HPr in *transparent lilac*, helices α1 and α4 of the A chain of IIA^{Man} in *blue*, and helices α2 and α3 of the B chain of IIA^{Man} in *red*.

thus His-175 is potentially available to transfer a phosphoryl group onto the incoming sugar located on the transmembrane IIC^{Man}-IID^{Man} complex. It is interesting to note that His-175 lies close to the upper edge of a deep V-shaped hydrophobic cleft at the bottom of which lies helix α3 of IIB^{Man}, with an outer rim of negatively charged residues (Asp-106, Asp-107, and Asp-108) provided by the A chain of IIA^{Man} and positively charged residues (Arg-172, Arg-181, Arg-204, and Lys-305) by IIB^{Man}. The walls of the cleft are formed by helices α1 and α4 of the A chain of IIA^{Man}, and the active site loop, helix α1, and the loops between strands β5 and β6 and between β6 and β7 of IIB^{Man}. It is tempting to speculate that this cleft comprises part of the binding site for the membrane-bound IIC^{Man}-IID^{Man} complex. In this regard, it is worth noting that IIAB^{Man} has been reported to form a stable complex with the transmembrane IIC^{Man}-IID^{Man} component of the mannose transporter with an apparent K_D of 5–10 nM (57), and a IIAB^{Man}-IIC^{Man}-IID^{Man} complex can be co-purified (58).

Probing the Role of Arg-172 in Complex Formation—The successful elimination of the non-productive complex as a consequence of the introduction of the phosphomimetic H10E mutation providing charge neutralization of Arg-172, strongly suggests a major role for Arg-172 in conjunction with phosphorylation of His-10 in modulating whether a productive or non-productive complex is formed. To probe the role of Arg-172 further, intermolecular NOEs involving the leucine (Leu-24, Leu-25, and Leu129), valine (Val-99 and Val-134), and methionine (Met-23 and Met-103) methyl groups of IIA^{Man} were analyzed for the following samples: IIA^{Man}-IIB^{Man}(H175E), IIA^{Man}-IIB^{Man}(R172Q), and IIA^{Man}(H10E)-IIB^{Man}(R172Q). A qualitative assessment of the proportion of productive to non-productive complexes in these samples relative to the wild-type IIA^{Man}-IIB^{Man} sample can be obtained by examining (*a*) the fraction of observed intermolecular NOEs attributable to the productive complex and (*b*) the ratio of the intermolecular NOE cross-peak intensities involving the methyl group of Met-103 of IIA^{Man} attributable to the productive and non-productive complexes (*cf.* Fig. 2, *top panels*). The latter has a value of ~0.8 for the wild-type sample. (Note this value cannot be converted to populations of the two species in the wild-type sample, because the NOE intensities are related not only to population but also to specific intermolecular interproton distances in the two complexes.)

The pattern of intermolecular NOEs observed for the IIA^{Man}-IIB^{Man}(H175E) sample is very similar to that of the wild-type IIA^{Man}-IIB^{Man} sample, with only ~15% of the intermolecular NOEs attributable to the productive complex compared with ~10% for the wild-type sample. The ratio of the cross-peak intensities for the productive to non-productive complexes is increased by ~1.2 relative to wild-type. These data indicate that the proportion of non-productive complex is only slightly decreased relative to wild type and, therefore, suggest that the H175E mutation does not provide adequate intramolecular charge neutralization of Arg-172. This finding may be relevant to the postulated role of the non-productive complex in transferring a phosphoryl group on to the incoming sugar on the transmembrane IIC^{Man}-IID^{Man} complex. In particular, this result may suggest that, once the phosphoryl group is transferred from His-10′ to His-175, the equilibrium between productive and non-productive complex may be shifted toward the non-productive complex if the intramolecular charge neutralization of Arg-172 by phosphorylated His-175 is less effective than the intermolecular charge neutralization by phosphorylated His-10′. This hypothesis may be supported by the observation that the side chain of Arg-172 is disordered in the crystal structure of *B. subtilis* IIB^{Lev} (49).

For the IIA^{Man}-IIB^{Man}(R172Q) sample, intermolecular NOEs corresponding to both productive and non-productive complexes were observed, but the fraction attributable to the

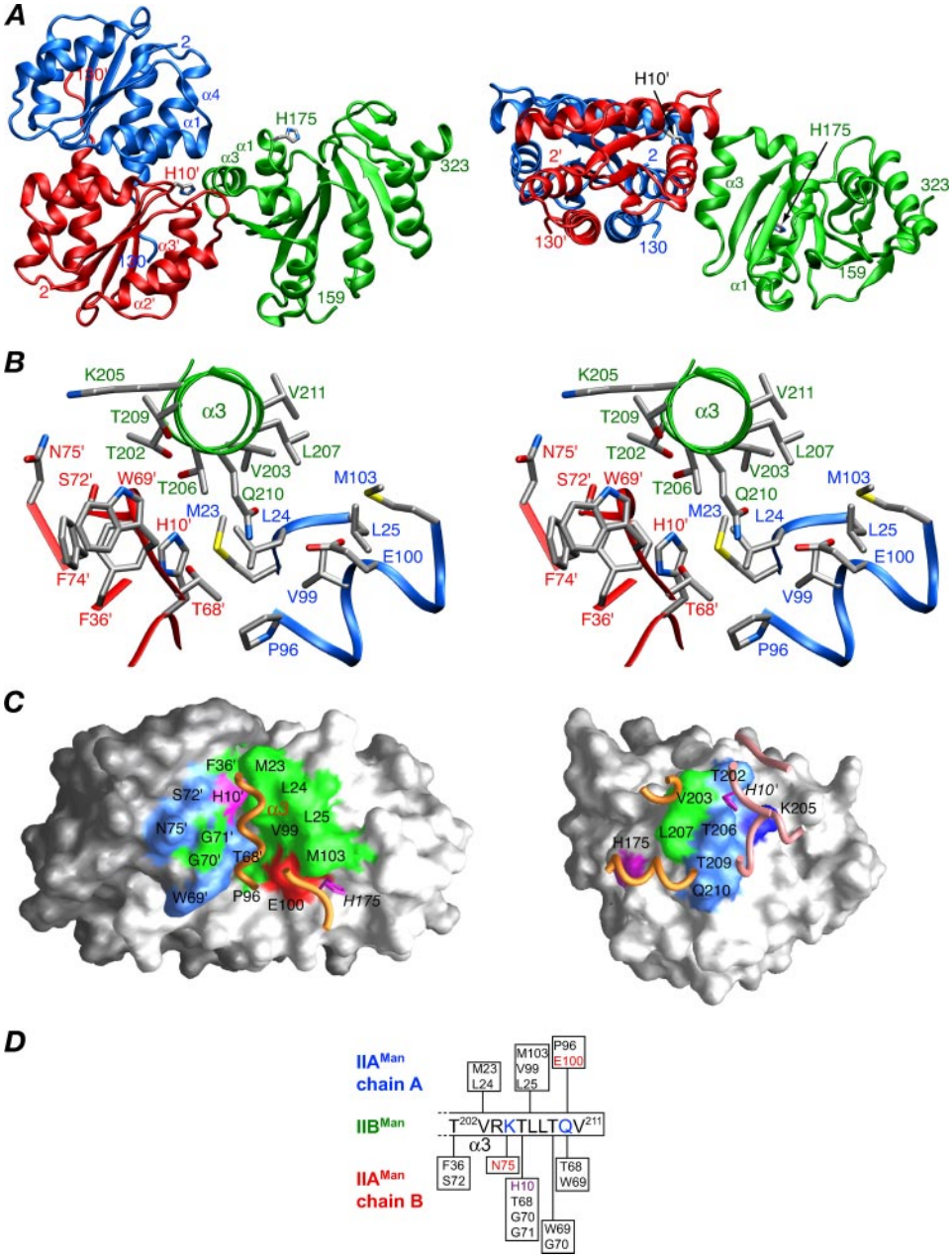

FIGURE 8. **The non-productive, phosphoryl transfer incompetent, IIA^{Man}-IIB^{Man} complex observed with wild-type IIA^{Man}.** *A*, ribbon diagram (*blue*, chain A of IIA^{Man}; *red*, chain B or IIA^{Man}; *green*, IIB^{Man}). The side chains of the active site histidines (His-10′ of IIA^{Man} and His-175 of IIB^{Man}, separated by a Cα–Cα distance of ~25 Å, are also shown. *B*, stereoview showing the detailed interactions at the interface. The color coding of the backbone chains (shown as *tubes*) is as in *A*, and the side-chain bonds are colored coded according to atom type (see Fig. 6 legend). *C*, interaction surfaces for the non-productive IIA^{Man}-IIB^{Man}. The *left* and *right panels* display the interaction surfaces on IIA^{Man} and IIB^{Man}, respectively, with the color coding as in Fig. 6*B*. *D*, diagrammatic representation of the intermolecular contacts with the active site His-10′ colored in *purple*, and residues involved in potential side chain-side chain intermolecular electrostatic interactions colored in *red* (acceptor) and *blue* (donor).

productive complex was increased to ~30%, and the ratio of the cross-peak intensities of productive to non-productive complexes was increased by ~5-fold relative to wild type. Thus, the population of productive complex in the IIA^{Man}-IIB^{Man}(R172Q) sample was increased substantially relative to the wild-type IIA^{Man}-IIB^{Man} sample. The R172Q mutation removes the positive charge of Arg-172 but still leaves a potentially unfavorable polar residue in the middle of the interface of the productive complex, thereby accounting for the continued presence of non-productive complex.

Finally, ~90% of intermolecular NOEs observed for the IIA^{Man}(H10E)-IIB^{Man}(R172Q) sample arise from the productive complex, and the few from the non-productive complex were extremely weak relative to their intensities in the wild-type sample. The ratio of NOE cross-peak intensities of productive to non-productive complexes for Met-103 was increased ~9-fold relative to wild type. Thus, the productive complex constitutes the major species. This result is consistent with the observation that IIB^{Man}(R172Q) can still be phosphorylated by IIA^{Man}, albeit somewhat less efficiently than wild-type IIB^{Man} (59).

Concluding Remarks—This report completes the structures of cytoplasmic complexes of the mannose branch of the PTS. The intriguing finding is that the nature of the IIA^{Man}-IIB^{Man} complex can be modulated by the presence or absence of charge neutralization between the active sites, and in particular of the guanidino group of Arg-172. With wild-type IIA^{Man}, two forms of complex with IIB^{Man} were observed: the predominant one arises from a non-productive complex in which the active site histidines (His-10′ and His-175) are separated by ~25 Å and therefore incompatible with phosphoryl transfer between IIA^{Man} and IIB^{Man}, whereas the minor one arises from a productive complex in which the active site histidines are in close proximity. Mutation of His-10′ of IIA^{Man} to a Glu to mimic histidine phosphorylation results in the exclusive formation (at the level of detection) of a productive complex that is fully consistent with the formation of a pentacoordinate phosphoryl transition state and in which the positive charge on the guanidinium group of Arg-172 is neutralized by interaction with the negative carboxylate group of H10E′. In the non-productive complex, Arg-172 and the active site His-175 of IIB^{Man} are fully exposed to solvent and potentially available to transfer a phosphoryl group to the sugar located on the cytoplasmic side of the IIC^{Man}-IID^{Man} transmembrane complex.

The structural transition between the productive and non-productive states is dramatic and involves a 90° rotation and concomitant 37-Å translation of IIB^{Man} relative to IIA^{Man}. The interaction surface on IIA^{Man} in the non-productive complex comprises a subset of residues located in the central region of the interaction surface employed in the productive complex, including the active site His-10′. Thus, the non-productive complex does not allow for the formation of a ternary HPr-IIA^{Man}-IIB^{Man} complex, because the interaction surface on IIA^{Man} used by IIB^{Man} is also a subset of the interaction surface on IIA^{Man} used by HPr. The interaction surface on IIB^{Man} in the productive and non-productive complexes also partially overlap insofar that the interaction surface in the non-productive complex comprises exclusively helix α3, which is used in a completely different set of interactions with IIA^{Man} in the productive complex.

The existence of the non-productive IIA^{Man}-IIB^{Man} complex may be fortuitous owing to the presence of a highly hydrophobic protrusion on the surface of IIB^{Man} formed by helix α3 that can readily fit in a groove between the two subunits of IIA^{Man}. Nevertheless, it seems likely that weak binding complexes with K_D values in the 0.1–2 mM range may be particularly susceptible to multiple alternative configurations arising from rather small changes at the interface. Indeed, two distinct quaternary structures resulting from a relatively small number of changes at an interface have been observed in the much tighter homodimeric complexes of the chemokine family where the CXC and CC chemokines have high sequence identity, the same monomer folds, but entirely different dimeric structures employing completely different interfaces (60).

Acknowledgments—We thank Alan Peterkofsky for providing the DNA template for IIB^{Man} and Dan Garrett for software support.

REFERENCES

1. Meadow, N. D., Fox, D. K., and Roseman, S. (1990) *Annu. Rev. Biochem.* **59,** 497–542
2. Siebold, C., Flükiger, K., Beutler, R., and Erni, B. (2001) *FEBS Lett.* **504,** 104–111
3. Deutscher, J., Francke, C., and Postma, P. W. (2006) *Microbiol Mol. Biol. Rev.* **70,** 939–1031
4. Legler, P. M., Cai, M., Peterkofsky, A., and Clore, G. M. (2004) *J. Biol. Chem.* **279,** 39115–39121
5. Van Montfort, R. L., Pijning, T., Kalk, K. H., Reizer, J., Saier, M. J., Thunnissen, M. M., Robillard, G. T., and Dijkstra, B. W. (1997) *Structure* **5,** 217–225
6. Garrett, D. S., Seok, Y.-J., Peterkofsky, A., Gronenborn, A. M., and Clore, G. M. (1999) *Nature Struct. Biol.* **6,** 166–173
7. Wang, G., Louis, J. M., Sondej, M., Seok, Y.-J., Peterkofsky, A., and Clore, G. M. (2000) *EMBO J.* **19,** 5635–5649
8. Cornilescu, G., Lee, B. R., Cornilescu, C., Wang, G., Peterkofsky, A., and Clore, G. M. (2002) *J. Biol. Chem.* **277,** 42289–42298
9. Williams, D. C., Cai, M., Suh, J.-Y., Peterkofsky, A., and Clore, G. M. (2005) *J. Biol. Chem.* **280,** 20775–20784
10. Cai, M., Williams, D. C., Wang, G., Lee, B. R., Peterkofsky, A., and Clore, G. M. (2003) *J. Biol. Chem.* **278,** 25191–25206
11. Suh, J.-Y., Cai, M., Williams, D. C., and Clore, G. M. (2006) *J. Biol. Chem.* **281,** 8939–8949
12. Williams, N., Fox, D. K., Shea, C., and Roseman, S. (1986) *Proc. Natl. Acad. Sci. U. S. A.* **83,** 3083–3086
13. Erni, B., Zanolari, B., and Kocher, H. P. (1987) *J. Biol. Chem.* **262,** 5238–5247
14. Erni, B., Zanolari, B., Graff, P., and Kocher, H. P. (1989) *J. Biol. Chem.* **264,** 18733–18741
15. Markovic-Housley, Z., Cooper, A., Lustig, A., Flükiger, K., Stolz, B., and Erni, B. (1994) *Biochemistry* **33,** 10977–10984
16. Nunn, R. S., Markovic-Housley, Z., Genoveso-Taverne, G., Flükiger, K., Rizkallah, P. J., Jansonius, J. N., Schirmer, T., and Erni, B. (1996) *J. Mol. Biol.* **259,** 502–511
17. Gutknecht, R., Flükiger, K., Lanz, R., and Erni, B. (1999) *J. Biol. Chem.* **274,** 6091–6096
18. Wehmeier, U. F., and Lengeler, J. W. (1994) *Biochim. Biophys. Acta* **1208,** 348–351
19. Martin-Verstraete, I., Debarbouille, M., Lier, A., and Rapoport, G. (1990) *J. Mol. Biol.* **214,** 657–661
20. Clore, G. M. (2000) *Proc. Natl. Acad. Sci. U. S. A.* **97,** 9021–9025
21. Schwieters, C. D., and Clore, G. M. (2001) *J. Magn. Reson.* **152,** 288–302
22. Goto, N. K., Gardner, K. H., Mueller, G. A., Willis, R. C., and Kay, L. E. (1999) *J. Biomol. NMR* **13,** 369–374
23. Delaglio, F., Grzesiek, S., Vuiser, G. W., Zhu, G., Pfiefer, J., and Bax, A. (1995) *J. Biomol. NMR* **6,** 277–293
24. Garrett, D. S., Powers, R., Gronenborn, A. M., and Clore, G. M. (1991) *J. Magn. Reson.* **95,** 214–220
25. Clore, G. M., and Gronenborn, A. M. (1991) *Ann. Rev. Biophys. Biophys. Chem.* **20,** 29–63
26. Clore, G. M., and Gronenborn, A. M. (1998) *Trends Biotechnol.* **16,** 22–34
27. Bax, A., Vuister, G. W., Grzesiek, S., Delaglio, F., Wang, A. C., Tschduin, R., and Zhu, G. (1994) *Methods Enzymol.* **239,** 79–105
28. Bax, A., Kontaxis, G., and Tjandra, N. (2001) *Methods Enzymol.* **339,** 127–174
29. Clore, G. M., Starich, M. R., and Gronenborn, A. M. (1998) *J. Am. Chem. Soc.* **120,** 10571–10572
30. Rückert, M., and Otting, G. (2000) *J. Am. Chem. Soc.* **122,** 7793–7797
31. Kay, L. E. (2005) *J. Magn. Reson.* **173,** 193–2007
32. Cai, M., Huang, Y., Zheng, R., Wei, S. Q., Ghirlando, R., Lee, M. S., Craigie, R., Gronenborn, A. M., and Clore, G. M. (1998) *Nat. Struct. Biol.* **5,** 903–909
33. Clore, G. M., Sukuraman, D. K., Nilges, M., Zarbock, J., and Gronenborn, A. M. (1987) *EMBO J.* **6,** 529–537
34. Nilges, M. (1993) *Proteins* **17,** 297–309
35. Cornilescu, G., Delaglio, F., and Bax, A. (1999) *J. Biomol. NMR* **13,** 289–302
36. Schwieters, C. D., Kuszewski, J., and Clore, G. M. (2006) *Progr. NMR Spect.* **48,** 47–62
37. Clore, G. M., and Bewley, C. A. (2001) *J. Magn. Reson.* **154,** 329–335
38. Clore, G. M., Nilges, M., Sukuraman, D. K., Brünger, A. T., Karplus, M., and Gronenborn, A. M. (1986) *EMBO J.* **5,** 2729–2735
39. Kuszewski, J., Gronenborn, A. M., and Clore, G. M. (1995) *J. Magn. Reson. Ser B* **106,** 92–96
40. Clore, G. M., Gronenborn, A. M., and Tjandra, N. (1998) *J. Magn. Reson.* **31,** 159–162
41. Nilges, M., Gronenborn, A. M., Brünger, A. T., and Clore, G. M. (1988) *Protein Eng.* **2,** 27–38
42. Clore, G. M., and Kuszewski, J. (2002) *J. Am. Chem. Soc.* **124,** 2866–2867
43. Grishaev, A., and Bax, A. (2004) *J. Am. Chem. Soc.* **126,** 7281–7292
44. Schwieters, C. D., and Clore, G. M. (2007*) J. Phys. Chem. B.* 10.1021/jp076244o
45. Quilin, M. L., and Matthews, B. W. (2000) *Acta Crystallogr. Sect. D Biol. Crystallogr.* **56,** 791–794
46. Schwieters, C. D., and Clore, G. M. (2001) *J. Magn. Reson.* **149,** 239–244
47. Nicholls, A, Sharp, K. A., and Honig, B. (1991) *Proteins* **11,** 281–296
48. Laskowski, R. A., MacArthur, M. W., Moss, D. S., and Thornton, J. M. (1993) *J. Appl. Crystallogr.* **26,** 283–291
49. Shauder, S., Nunn, R. S., Lanz, R., Erni, B., and Schirmer, T. (1998) *J. Mol. Biol.* **276,** 591–602
50. Oriss, G. L., Erni, B., and Schirmer, T. (2003) *J. Mol. Biol.* **327,** 1111–1119
51. Suh, J.-Y., Iwahara, J., and Clore, G. M. (2006) *Proc. Natl. Acad. Sci. U. S. A.* **104,** 3153–3158
52. Cantor, C. R., and Schimmel, P. R. (1980) in *Biophysical Chemistry Part III:*

The Behavior of Biological Macromolecules, Chapter 18, pp. 979–1018, W. H. Freeman & Co., San Francisco
53. Jones, S., and Thornton, J. M. (1996) *Proc. Natl. Acad. Sci. U. S. A.* **93,** 13–20
54. Begley, G. S., Hansen, D. E., Jacobsen, G. R., and Knowles, J. R. (1982) *Biochemistry* **21,** 5552–5556
55. Mueller, E. G., Khandekar, S. S., Knowles, J. R., and Jacobsen, G. R. (1990) *Biochemistry* **29,** 6892–6896
56. Hollfelder, F., and Herschlag, D. (1995) *Biochemistry* **34,** 12255–12264
57. Mao, Q., Schunk, T., Flükiger, K., and Erni, B. (1995) *J. Biol. Chem.* **270,** 5258–5265
58. Rhiel, E., Flükiger, K., Wehrli, C., and Erni, B. (1994) *Biol. Chem. Hoppe-Seyler* **375,** 551–559
59. Gutknecht, R., Lanz, R., and Erni, B. (1998) *J. Biol. Chem.* **273,** 12234–12238
60. Clore, G. M., and Gronenborn, A. M. (1995) *FASEB J.* **9,** 57–62
61. Clore, G. M., and Garrett, D. S. (1999) *J. Am. Chem. Soc.* **121,** 9008–9012
62. Clore, G. M., Gronenborn, A. M., and Bax, A. (1998) *J. Magn. Reson.* **133,** 216–221
63. Vriend, G., and Sander, C. (1993) *J. Appl. Crystallogr.* **26,** 47–60